Nuclear Engineering and Technology 53 (2021) 2364–2370

Contents lists available at ScienceDirect

Nuclear Engineering and Technology

journal homepage: www.elsevier.com/locate/net

Original Article

Efficiency calculation of the ^{n}MCP with ^{10}B doping based on mathematical models

Jianqing Yang [a, b, c], Jianrong Zhou [b, c, d, *], Lianjun Zhang [b, c, e], Jinhao Tan [b, c, e], Xingfen Jiang [b, c], Jianjin Zhou [b, c], Xiaojuan Zhou [b, c], Linjun Hou [a], Yushou Song [e], XinLi Sun [a], Quanhu Zhang [a, **], Zhijia Sun [b, c, d, ***], Yuanbo Chen [b, c, d]

[a] Xi'an Research Inst. of Hi-Tech, 710025, Xian, China
[b] Spallation Neutron Source Science Center, Dongguan, 523803, Guangdong, China
[c] State Key Laboratory of Particle Detection and Electronics, Institute of High Energy Physics, Chinese Academy of Sciences, Beijing, 100049, China
[d] University of Chinese Academy of Sciences, Beijing 100049, China
[e] Harbin Engineering University, Harbin, Heilongjiang, 150000, China

ARTICLE INFO

Article history:
Received 12 May 2020
Received in revised form
23 December 2020
Accepted 25 January 2021
Available online 2 February 2021

Keywords:
^{n}MCP
Detection efficiency
Mathematical model

ABSTRACT

The ^{n}MCP (Neutron sensitive microchannel plate) combined with advanced readout electronics is widely used in energy selective neutron imaging because of its good spatial and timing resolution. Neutron detection efficiency is a crucial parameter for the ^{n}MCP. In this paper, a mathematical model based on the oblique cylindrical channel and elliptical pore was established to calculate the neutron absorption probability, the escape probability of charged particles and overall detection efficiency of ^{n}MCP and analyze the effects of neutron incident position, pore diameter, wall thickness and bias angle. It was shown that when the doping concentration of the ^{n}MCP was 10 mol%, the thickness of ^{n}MCP was 0.6 mm, the detection efficiency could reach maximum value, about 24% for thermal neutrons if the pore diameter was 6 μm, the wall thickness was 2 μm and the bias angle was 3 or 6°. The calculated results are of great significance for evaluating the detection efficiency of the ^{n}MCP. In a subsequent companion paper, the mathematical model would be extended to the case of the spatial resolution and detection efficiency optimization of the coating ^{n}MCP.

1. Introduction

CSNS(China Spallation Neutron Source) with a power of 100 kW and a pulse repetition frequency of 25 Hz is first pulsed neutron source in China and an Energy resolved Neutron Imaging Instrument(ERNI) is planning to be built at CSNS [1,2]. The ^{n}MCP detector is a favorable choice for ERNI because of its high spatial resolution of sub-15μm [3] and timing resolution of sub-microsecond [4]. MCP is a thin glass plate composed of millions of parallel channels in a honeycomb-like packed structure [5]. The standard MCP is not sensitive to neutrons which can be realized by doping neutron sensitive nuclides (such as ^{6}Li, ^{10}B and ^{nat}Gd) in the glass substrate [6,7]. The ^{n}MCP detector was constructed by A.S.Termsin et al. based on the ^{10}B doped ^{n}MCP and Timepix readout electronics. A series of experiments were performed by them at SNS of USA and ISIS of UK [8,9], and the ^{n}MCP detector has been determined to be the detector for IMAT instrument at ISIS and VENUS instrument at SNS.

Neutron detection efficiency is a key parameter for evaluating the ^{n}MCP detector. Anton Tremsin et al. proposed an theoretical model for ^{10}B doped ^{n}MCP of the square channel geometry [10]. Neutron absorption probability, the probability of secondary charged particles escaping into open channels and the total neutron detection efficiency were calculated under different neutron incident angles and position coordinates, as well as different pore diameters and wall thicknesses respectively. Wang S

* Corresponding author. Dongguan, China.
** Corresponding author. Xian, China.
*** Corresponding author. Beijing, China.
E-mail addresses: zhoujr@ihep.ac.cn (J. Zhou), zhangqh102@sina.com (Q. Zhang), sunzj@ihep.ac.cn (Z. Sun).

https://doi.org/10.1016/j.net.2021.01.026

et al. calculated the detection efficiency of the ^{n}MCP doped and coated by ^{10}B and natural Gd with Monte-Carlo method [11]. Z.W.Ma et al. simulated the detection efficiency and the spatial resolution of ^{10}B doped ^{n}MCP in various geometrical configurations [12]. J. Pan et al. established a mathematical model to calculate the neutron absorption efficiency of natural Gd doped under different neutron incident angles and position coordinates [13].

In this paper, the mathmatical models were constructed to calculate the neutron absorption probability, the probability of secondary charged particles escaping into channels and the total detection efficiency. The results are valuable for evaluating the detection efficiency of the ^{n}MCP.

2. Mathematical model of neutron detection efficiency

When an incident neutron interacted with a ^{10}B atom, the nuclear reaction was shown in fomula (1). In the glass substrate, this nuclear reaction had 94% probability of producing 0.83 MeV of ^{7}Li particles with a range of 1.91 μm and 1.47 MeV of α particles with a range of 3.54 μm and 6% probability of generating 1.0 MeV of ^{7}Li particles with a range of 2.15 μm and 1.8 MeV of α particles with a range of 4.23 μm [10].

$$\begin{aligned} &^{10}\mathrm{B}+\mathrm{n}\rightarrow{}^{7}\mathrm{Li}(1.0\mathrm{MeV})+{}^{4}\mathrm{He}(1.8\mathrm{MeV})\ 6\% \\ &^{10}\mathrm{B}+\mathrm{n}\rightarrow{}^{7}\mathrm{Li}(0.83\mathrm{MeV})+{}^{4}\mathrm{He}(1.47\mathrm{MeV})+\gamma(0.48\mathrm{MeV})\ 94\% \end{aligned} \tag{1}$$

$$P = P_1 \times P_2 \times P_3 \tag{2}$$

The neutron detection efficiency was shown in formula (2), where P_1 was the neutron absorption probability, P_2 represented the probability of the secondary charged particles escaping into channels, P_3 was the probability of the avalanche signal being detected, which was generally equal to 1 [10]. In this simulation, the neutron energy was 0.0253eV. The incidence direction of the neutron beam was perpendicular to the surface of ^{n}MCP and the neutron beam was a uniform beam of a hexagon with a length of pore diameter(shown in Fig. 1).

2.1. Mathematical model of oblique cylinder channel and elliptical pore

The manufacturing process of the MCP included the following several steps. Firstly, the mono-fiber glasses were drawn, and were stacked into the multi-fiber glass. Secondly, the multi-fiber glass was pressed and fused into a boule. Thirdly, the boule was sliced according to the bias angle, and the slices were ground and polished. Next, the polished slices were subjected to chemical processing, hydrogen reduction and electrode evaporation. Finally, the test and inspection would be done and MCP could be gotten. Considering the manufacturing process of the MCP, the oblique cylindrical channels and elliptical pores were obtained when cylindrical mono-fibers were sliced at a bias angle. As we know, the reason was that an elliptical section curve was obtained when a plane with a bias angle sliced a cylinder. The geometric parameters of ^{n}MCP were defined as follows, L was the thickness of the ^{n}MCP, d was the pore diameter, w was the wall thickness, and θ was the bias angle.

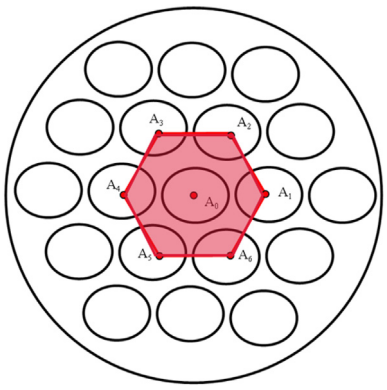

Fig. 1. Schematic diagram of the hexagonal neutron beam.

In order to describe this elliptical pore, the ellipse focus coordinates and the sum of two distances to the focal points, which was the major axis of the ellipse needed to be calculated. Two spheres were placed inside the cylinder which were tangent to the side and the elliptical plane of the cylinder respectively. Side view of oblique cylindrical channel and elliptical pore were shown in Fig. 2. The diameter of the cylinder was d and the bias angle was θ in Fig. 2 (a). Thus, PM=NQ=d/2, <PMO=<QNO = θ and the coordinates of tangent point P and Q (elliptical focus) were (-d/2tanθ, d/2tanθ). The distances between point H on the ellipse and two focus were HP and HQ. The elliptical major axis length was equal to HP + HQ=HE + HF = EF = MN = d/cosθ. The elliptical minor axis length was equal to d. So the equation of the elliptical pore was shown in formula (3).

$$\begin{aligned} &\sqrt{\left(x+\frac{d}{2}\tan\theta\right)^2+y^2}+\sqrt{\left(x-\frac{d}{2}\tan\theta\right)^2+y^2}=\frac{d}{\cos\theta} \\ &x^2+y^2=\frac{d^2}{4}(\theta=0^\circ) \end{aligned} \tag{3}$$

2.1. Mathematical model of neutron absorption probability P_1

The probability of neutron absorption was given by formula (4), where L_{eff} was the effective absorption length of neutrons within the ^{n}MCP substrate, $N_{^{10}B}$was the number of ^{10}B atoms per unit volume of the ^{n}MCP substrate. σ was the cross section (3844 b) for the ^{10}B(n,α) [14].$N_{^{10}B}$ could be calculated by formula(4). Where, ρ was the density of ^{n}MCP, $A_{^{10}B}$was the molecular mass of $^{10}B_2O_3$, N_A was Avogadro's number, $w_{^{10}B}$was the mass percentage of $^{10}B_2O_3$, $w_i^{mole}$was the mole percentage of material i.

$$P_1 = 1-\exp\left(-L_{eff}N_{^{10}B}\sigma\right), N_{^{10}B}=\frac{\rho\cdot w_{^{10}B}}{A_{^{10}B}}\cdot N_A, w_{^{10}B}=\frac{A_{^{10}B}w_{^{10}B}^{mole}}{\sum_i A_i w_i^{mole}} \tag{4}$$

$$\begin{aligned} &L_i=\frac{2}{\cos\theta}\sqrt{\frac{d^2}{4}-(y-y_i)^2} \\ &x_{\max}=x_i+\frac{L}{2}\tan\theta+\frac{L_i}{2}\quad x_{r1}=x_i+\frac{L}{2}\tan\theta-\frac{L_i}{2} \\ &x_{\min}=x_i-\frac{L}{2}\tan\theta-\frac{L_i}{2}\quad x_{r2}=x_i-\frac{L}{2}\tan\theta+\frac{L_i}{2} \end{aligned} \tag{5}$$

L_{eff} was related to the neutron incident position, ^{n}MCP thickness, pore diameter and wall thickness, bias angle. A schematic diagram of the neutron passing through single channel was shown in Fig. 3. The central coordinates of the channel were (x_i,y_i). In the XOY plane, the section curve of the ^{n}MCP channel was elliptical, and the neutron incidence point was $P(x, y)$. The elliptical chord length

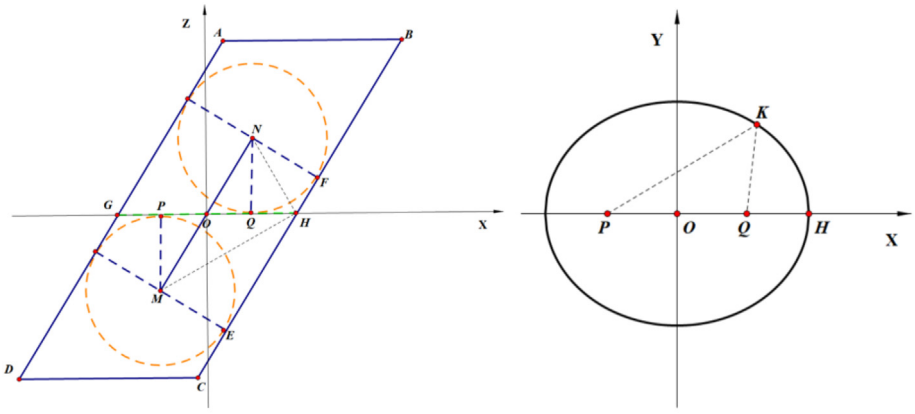

(a) side view (b) elliptical pore

Fig. 2. Side view of oblique cylindrical channel and elliptical pore.

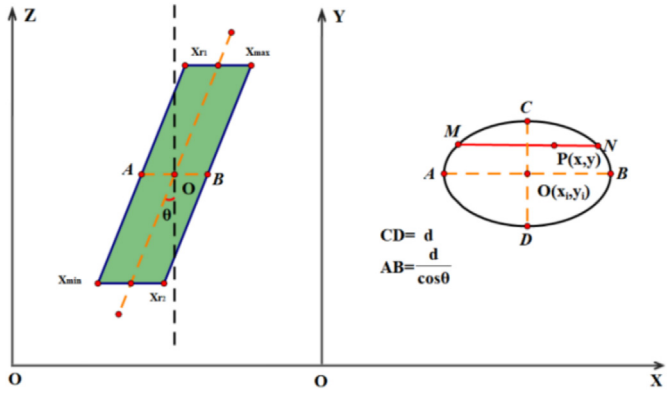

Fig. 3. Geometric model of individual channel.

MN was equal to L_i in the x direction which could be calculated according to the elliptic formula (5). In the XOZ plane, the side view of ^{n}MCP channel was parallelogram whose four vertex coordinates were x_{r1}, x_{max}, x_{min} and x_{r2}. If the neutron incident point $P(x,y)$ satisfied the condition in formula (6), it indicated that the neutron would pass through the channel. The neutron trajectory length L_p within a channel could be expressed as formula (7). When the neutron passed through *n* channels, the effective absorption length could be calculated according to formula (8), where the L_{pi} was the neutron trajectory length through the channel *i*.

$$x_{max} > x > x_{min}, y_i + \frac{d}{2} > y > y_i - \frac{d}{2} \tag{6}$$

$$x_{r2} > x_{r1} \quad x_{r1} > x_{r2}$$

$$L_p = \begin{cases} \dfrac{x - x_{min}}{\tan\theta} (x_{min} < x < x_{r1}) \\ L (x_{r1} < x < x_{r2}) \\ \dfrac{x_{max} - x}{\tan\theta} (x_{r2} < x < x_{max}) \end{cases} \qquad L_p = \begin{cases} \dfrac{x - x_{min}}{\tan\theta} (x_{min} < x < x_{r2}) \\ \dfrac{L_i}{\sin\theta} (x_{r2} < x < x_{r1}) \\ \dfrac{x_{max} - x}{\tan\theta} (x_{r1} < x < x_{max}) \end{cases} \tag{7}$$

$$L_{eff} = L - \sum_{0}^{n} L_{pi} \tag{8}$$

2.2. Mathematical model of the escape probability P_2

When neutrons were captured by ^{10}B, α particles and ^{7}Li particles were produced, both of which emitted in opposite directions and had two ranges respectively. It was shown in Fig. 4 (a) that when the neutron was captured at point A, the possible positions of α particles and ^{7}Li particles were uniformly distributed on the imaginary escape spherical surface with point A as the spherical center and the ranges as radii. The probability of alpha or ^{7}Li particle escaping into an open MCP channel is the ratio of the spherical surface contained inside an open channel to the total spherical surface area [10]. In this paper, a C++ program was written to calculate the escape probability P_2. First, the scattered points, which represented the possible positions of particles and were in accordance with the uniform distribution, were generated on the imaginary spherical surface. Second, the number of scattered points within the open channel were counted. The model of judging whether the particles escaped into the open channels could be simplified into judging whether the scattered points were in the elliptic pore of the XOY plane after the focal coordinates of the elliptical pore moved ztanθ in the x direction (shown in Fig. 4 (b)). Finally, the probability P_2 of the corresponding neutron absorption positions would be obtained by dividing this number by the total number of scattered points on the imaginary spherical surface.

The flow chart of the P_2 calculation was shown in Fig. 5. The escape probability of α particles of 3.54 and 4.23 μm ranges, and ^{7}Li particles of 1.91 and 2.15 μm ranges were expressed as $P_2^{\alpha_1}$,$P_2^{\alpha_2}$, $P_2^{Li_1}$ and $P_2^{Li_2}$. The escape probability of α particles and ^{7}Li particles could be calculated respectively as formula (9). In order to calculate the total escape probability P_2 of these two particles, it was necessary to produce scattered points of ^{7}Li particle in the opposite direction while the scattered points of α particle were generated. This escape probability $P_2^{Li-\alpha_1}$ was the probability of α particles with 3.54 μm ranges or ^{7}Li particles with 1.91 μm ranges escaping into channels. The escape probability $P_2^{Li-\alpha_2}$ was the probability of α particles with 4.23 μm ranges or ^{7}Li particles with 2.15 μm ranges escaping into channels. The total escape probability could be

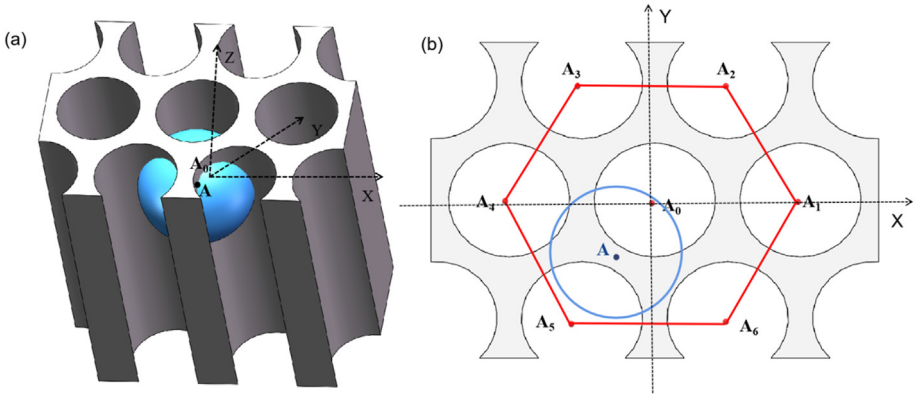

Fig. 4. (a) The 3D schematic diagram of the escape sphere of particles (b) Projection in the XOY plane.

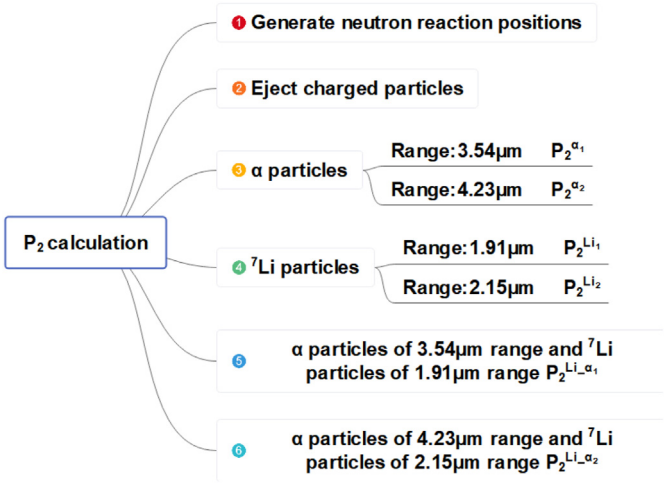

Fig. 5. Flow chart of P_2 calculation.

calculated as formula (9).

$$\begin{aligned} P_2^{\alpha} &= 0.94P_2^{\alpha_1} + 0.06P_2^{\alpha_2} \\ P_2^{Li} &= 0.94P_2^{Li_1} + 0.06P_2^{Li_2} \\ P_2 &= 0.94P_2^{Li-\alpha_1} + 0.06P_2^{Li-\alpha_2} \end{aligned} \tag{9}$$

3. Calculation of neutron detection efficiency *P*

The thickness of nMCP was set to 0.6 mm considering that the detection efficiency was required to be larger than 20% for thermal neutrons at CSNS [15] and the spatial resolution would become worse with the thickness [12]. In light of the ^{n}MCP manufacturability and mechanical stability, 10 mol% ^{10}B doping was currently achievable level [10], the pore diameter was no less than 6 μm, and the wall thickness was no less than 2 μm. The bias angle was necessary to inhibit the ion feedback. Thus, the doping concentration of B_2O_3 was 10%, L was 0.6 mm, d was 6–10 μm, w was 2–10 μm, θ was 0–12° in this calculation.

3.1. Probability $P_1(x,y)$ of neutron absorption

When L = 0.6 mm, d = 8 μm, w = 2 μm and θ = 0°, 0.5°, and 6°, two-dimensional spatial distributions of single neutron absorption probability were shown in Fig. 5. It was shown in Fig. 6 (a) that when θ = 0, if the neutron incidence position was inside the ellipse A_0, A_1, A_2, A_3, A_4, A_5 and A_6, the absorption probability was 0. And if the neutron incidence position was outside the ellipse A_0, A_1, A_2, A_3, A_4, A_5 and A_6, the corresponding probability P_1 was a fixed value, 0.618 because the effective absorption length was L=0.6 mm. Fig. 6 (b) showed that when θ = 0.5, there were two parts whose absorption probabilities were relatively large including the regions which were close to minor axis vertex between ellipses and two narrow-band regions whose width was 0.66 μm and effective lengths were 0.6 mm. At the same time, the channel with the coordinate center (0,0) was compressed in the x direction because of the bias angle. Fig. 6 (c) showed that when θ = 6°, there were still these two narrow-band regions where the absorption probabilities were largest. The bias angle was so large that the entire incidence plane could be detected.

3.2. Escape probability $P_2(x,y)$ of α and ^{7}Li reaction products

There was 94% probability of producing α particles with 3.54 μm range and ^{7}Li particles with 1.91 μm ranges. These two ranges were taken as an example to calculate $P_2(x,y)$. When L = 0.6 mm, d = 8 μm, w = 2 μm, θ = 6, the 2D spatial distribution of $P_2^{\alpha_1}(x,y)$,$P_2^{Li_1}(x,y)$ and$P_2^{Li-\alpha_1}(x,y)$ were shown in Fig. 7. Fig. 7 (a) showed that the escape probability$P_2^{\alpha_1}$in the middle part of the three channels and two channels was larger than that in other parts. Fig. 7 (b) showed that the escape probability$P_2^{\alpha_1}$in the middle part of the two channels was larger than that in other parts, there exsisted three layers of approximate hexagonal regions which had a decreasing efficiency in the middle part of the three channels and the lowest efficiency appeared right in the center among three channels because ^{7}Li had a shorter range compared with α particles.

The total escape probability $P_2^{Li-\alpha_1}$ was shown in Fig. 7 (c) which showed that the greatest probability appeared in the elliptical rings around the channels because the particles produced in this region were the easiest to enter the channels. It was the reason why the coated ^{n}MCP was developed in recent years. The coated ^{n}MCP was manufactured by coating 0.1–5 μm thick neutron sensitive layer to the inner wall of the channel which could improve the detection efficiency of the ^{n}MCP [16]. However, the coated ^{n}MCP is still in the research and development stage because it is not so long since the ALD coated technology was applied to the fabrication of the coated ^{n}MCP. At present, the doped ^{n}MCP is a more mature scheme compared with the coated ^{n}MCP.

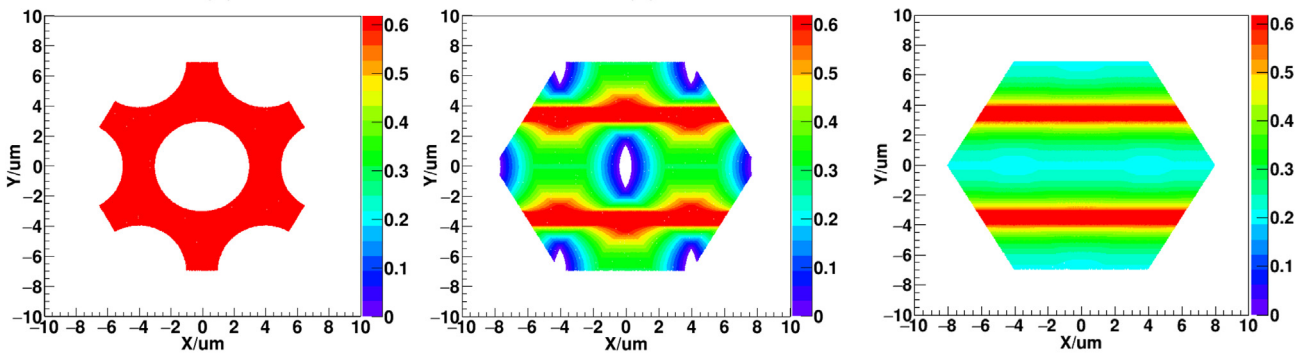

Fig. 6. 2D distribution of neutron absorption probability $P_1(x,y)$.

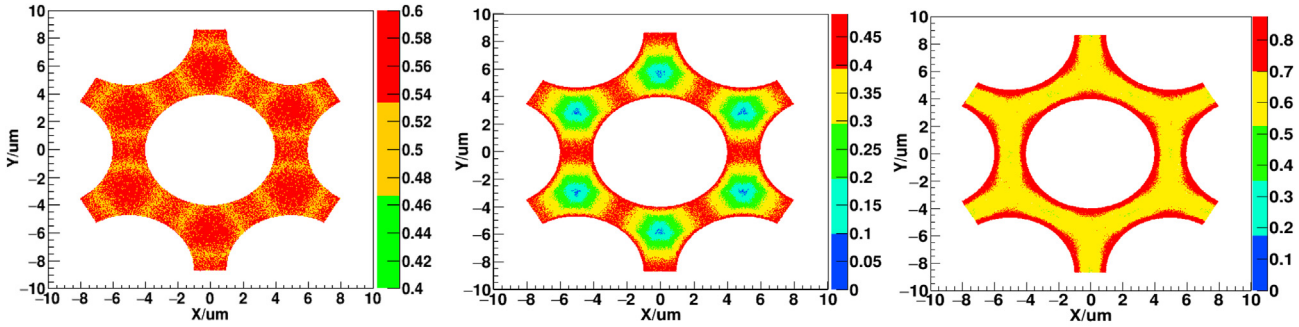

Fig. 7. 2D distribution of escape probabilities $P_2^{\alpha_1}$, $P_2^{Li_1}$ and $P_2^{Li-\alpha_1}$ ($\theta = 6$).

3.3. Neutron detection efficiency P

When L = 0.6 mm, $\theta = 6$, three average efficiencies P_1, P_2 and P with different pore diameters and wall thicknesses were shown in Fig. 8. It could be seen from Fig. 8 (a) that the average absorption probability P_1 increased with the increase of the wall thickness and decrease of the pore diameter. The reason was that when the wall thickness increased and the pore diameter decreased, the proportion of the substrate area became larger, which led to the increase of the absorption probability P_1. Fig. 8 (b) showed the average escape probability P_2 decreased with the increase of wall thickness, increased slightly with the increase of the pore diameter. The

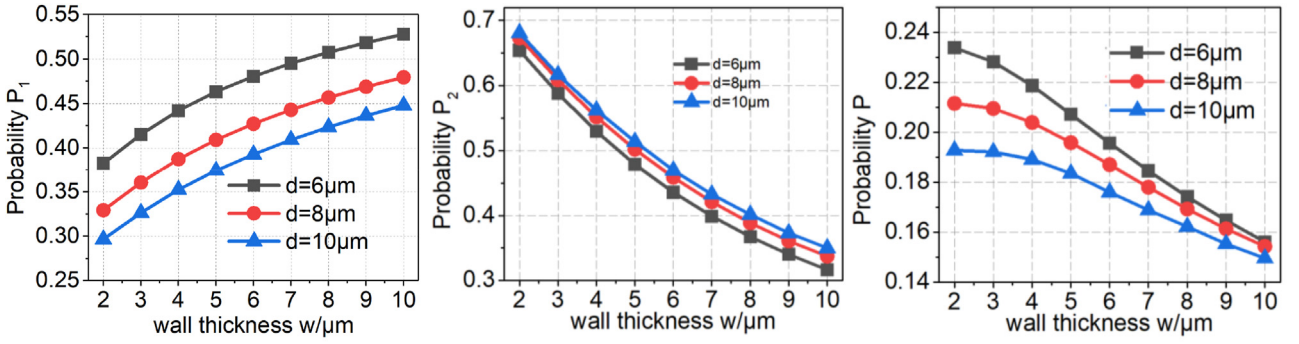

Fig. 8. Three average efficiencies P_1, P_2 and P with the pore size and wall thickness.

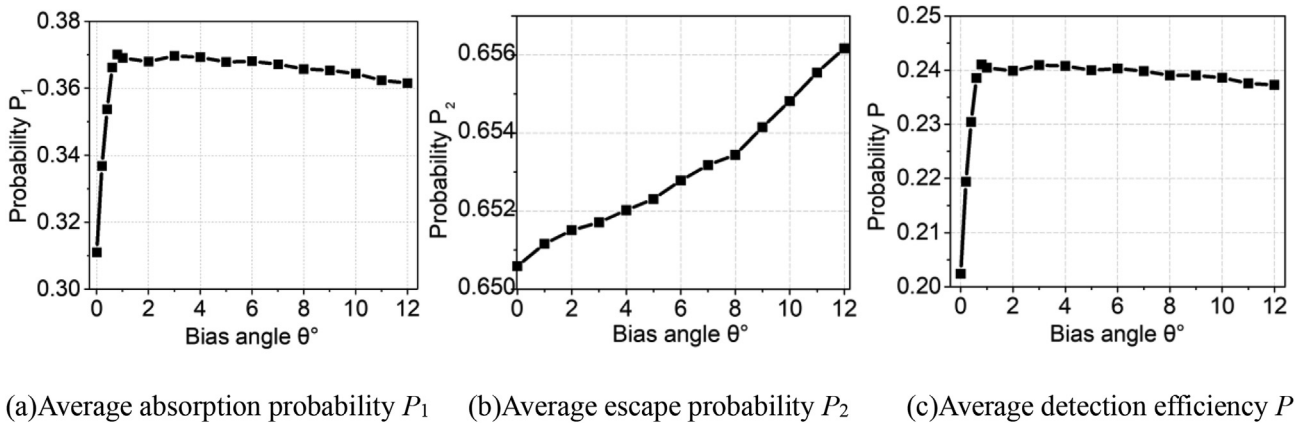

Fig. 9. Three average efficiencies P_1, P_2 and P with the bias angle θ

reason was that the ranges of secondary charged particles were fixed, fewer particles could enter the channel when the wall thickness increased. It could be seen from Fig. 8 (c) that the average value of the total detection efficiency P decreased with the increase of the wall thickness and the pore diameter. Therefore, the geometric parameters of d = 6 μm and w = 2 μm for the ^{10}B doped nMCP should be selected if the higher detection efficiency was required. The detection efficiency of the ^{n}MCP detector based on the ^{10}B doped ^{n}MCP was measured by Tremsin, A.S. and it reached almost 21% for thermal neutrons [17]. The detection efficiency calculated in this paper agreed well with the measured value by Tremsin, A.S. The results verify the validation of the calculation model in this paper.

When L = 0.6 mm, w = 6 μm and d = 2 μm, three average efficiencies P_1, P_2 and P of different bias angles were shown in Fig. 8. The average absorption probability P_1 increased rapidly with the bias angle from 0 to 1. The reason was that the neutrons, which penetrated the ^{n}MCP directly when the bias angle was 0 were detected when the bias angle was 1 so that the probability increased rapidly. Fig. 9 (b) showed that as the bias angle increased, the average escape probability P_2 increased with the bias angle in a very small range. The reason was that as the angle increased, the length of major axis of the ellipse increased resulting in more particles entering the channel. It could be seen from Fig. 9 (c) that the average detection efficiency P started to increase rapidly with the bias angle from 0 to 1, and was very stable when the bias angle varied from 1° to 12°. It should be noted that the positive ions produced at the output of the rear plate can reach the input of the front plate during the use of MCP. This is called ion feedback. To inhibit the ion feedback, the bias angles (3°/13° or 6°/6°) were commonly used to provide a sufficiently large directional change for MCP chevrons [18]. Thus, the bias angle can be 3° or 6° for the nMCP.

4. Conclusion

In this paper, the oblique cylindrical channel model and the elliptic equation of pore were established considering the manufacturing process of the ^{n}MCP. The neutron absorption probability P_1, the escape probability P_2 and the overall detection efficiency were calculated according to the mathematical models. The results are helpful for evaluating detection efficiency of the ^{n}MCP under the condition of different geometrical parameters. In the next research, the mathematical model would be extended to the case of the spatial resolution and detection efficiency calculation of the coating ^{n}MCP and the experiments of ^{10}B doped ^{n}MCP detector including detection efficiency and neutron-gamma discrimination will be performed at CSNS.

Declaration of competing interest

The authors declare that they have no known competing financial interests or personal relationships that could have appeared to influence the work reported in this paper.

Acknowledgement

This work was supported by the National Key R&D Program of China [Grant No. 2017YFA0403702], the National Natural Science Foundation of China [Grant No. 11635012, 11775243, U1832119], Youth Innovation Promotion Association CAS, Guangdong Basic and Applied Basic Research Foundation (Grant No. 2019A1515110217).

References

[1] H. Chen, X.L. Wang, China's first pulsed neutron source[J], Nat. Mater. 15 (7) (2016) 689–691.
[2] J.R. Zhou, Z.J. Sun, B. Liu, et al., Neutron beam monitor based on a boron-coated GEM[J], Chin. Phys. C (7) (2011) 668–674.
[3] A.S. Tremsin, J.V. Vallerga, et al., On the possibility to image thermal and cold neutron with sub-15 μm spatial resolution, Nucl. Instrum. Methods Phys. Res. Sect. A Accel. Spectrom. Detect. Assoc. Equip. 592 (3) (2008) 374–384.
[4] Tremsin, A. S., Feller, et al. High efficiency thermal neutron imaging with sub-microsecond timing resolution. In 2006 IEEE Nuclear Science Symposium Conference Record (Vol. 1, pp. 193-198). IEEE..
[5] W.B. Feller, R.G. Downing, et al., Neutron field imaging with microchannel plates[J], Proc. Soc. Photo Opt. Instrum. Eng. (4141) (2000) 291–302.
[6] J.V. Vallerga Siegmund, et al., High spatial resolution neutron sensing micro-channel plate detectors, Nuclear Instruments andMethods in Physics Research A 576 (2007) 178–182.
[7] J.V. Siegmund, A. Martin Vallerga, et al., A high spatial resolution event counting neutron detector using microchannel plates and cross delay line readout, Nucl. Instrum. Methods Phys. Res. 579 (1) (2007) 188–191.
[8] A.S. Tremsin, J.V. Vallerga, et al., On the possibility to image thermal and cold neutron with sub-15μm spatial resolution[J], Nucl. Instrum. Methods Phys. Res. (592) (2008) 374–384.
[9] W. Kockelmann, G. Frei, et al., Energy-selective neutron transmission imaging at a pulsed source[J], Nucl. Instrum. Methods Phys. Res. 578 (2) (2007) 421–434.
[10] A.S. Tremsin, W.B. Feller, et al., Efficiency optimization of microchannel plate (MCP) neutron imaging detectors. 1. Square channels with B-10 doping[J], Nucl. Instrum. Methods Phys. Res. (539) (2005) 278–311.
[11] S. Wang, H. Li, et al., Optimal calculation of detection efficiency for thermal neutron sensitive microchannel plate[J], Acta Phys. Sin. 64 (10) (2015) 102801.
[12] Z.W. Ma, J.R. Wang, et al., Monte Carlo simulation of 10B doped thermal neutron sensitive microchannel plate[J], J. Instrum. 13 (10) (2018) T10002.
[13] J. S. Pan S, Y.G. Yang, et al., High detection efficiency neutron sensitive microchannel plate[J], J. Instrum. (8) (2013) P01015.
[14] A.D. Carlson, The neutron cross section standards, evaluations and applications[J], Metrologia 48 (6) (2011) S328.

[15] T. Jinhao, Y. Jianqing, et al., Simulation of nMCP detector for time of flight neutron imaging, Progress Report on China Nuclear Science & Technology (2019) 2 (in Chinese).
[16] N.H. Lu, Y.G. Yang, et al., Neutron detector design based on ALD coated MCP[J], physics procedia (26) (2012) 61–69.
[17] O.H. Siegmund, Vallerga, et al., A high spatial resolution event counting neutron detector using microchannel plates and cross delay line readout, Nucl. Instrum. Methods Phys. Res. Sect. A Accel. Spectrom. Detect. Assoc. Equip. 579 (1) (2007) 188–191.
[18] J. Pan, J. Lv, et al., Ion feedback suppression for microchannel plate applied to third generation image intensifiers, Chin. J. Electron. 19 (4) (2010) 757–762.